

Theoretical-experimental thermal behavior of facade cladding mortars on hollow concrete block walls containing phase change materials

Abstract

In this study, we investigated the ability of the continuous active infrared thermography (IRT) technique to evaluate the behavior of phase change materials (PCM) added to cement-lime external cladding mortars (CLCM) applied over hollow concrete block walls. Three test specimens, namely, SP0, SP4, and SP8, were built. The first was coated with a 10 mm thick CLCM with no mixture of PCM. The other two specimens were coated with CLCM of the same thickness; however, the CLCM contained 4% and 8% PCM, considering the cement-PCM ratio by mass. A heat source of 1000 W was positioned to simulate the solar incidence on the hottest day and time of the year 2023 at the coordinates shown. The first thermogram was obtained from each specimen at time 00':00'' when starting the test. Then, when significant changing in temperature occurred, a new fixed image was taken from continuous acquisition. The internal computer chronometer measured the time required to increase the temperature of the surface of interest by 1.5 °C (± 0.2 °C), thrice for each specimen. The results indicated that the active IRT technique was useful for evaluating PCM behavior under laboratory conditions. However, real facades with similar materials must be evaluated to verify the performance of the technique in an open environment with large panels.

Keywords: Phase change material; Coating mortar; Cladding mortar; Hollow concrete block wall; Infrared thermography

1 Introduction and background

Using advanced materials has increased since the 21st century owing to the necessity of reducing energy consumption in various sectors of society. In civil construction, the use of phase-change materials (PCM) on building facades is an alternative technique for reducing energy consumption for heating or cooling [1,2]. However, in certain countries, particularly the least developed ones, technological advances require more time between their development and effective application in the construction industry. This factor hinders tracking the efficiency of a product during its evolution, from its first application until further

development, depending on the results obtained during its useful life. The trends and challenges in energy consumption worldwide between 1985 and 2050 have been documented, and countries with extreme climates possess a better opportunity to use PCM to reduce energy consumption for heating and cooling buildings [1,3].

1.1 PCM types and application

Recently, Zhan et al. reviewed PCM applications on plates and their effects in zones with high temperature levels [4]. Problems may arise when PCM are incorporated in mortars or stuccos used to cover masonry facades because they can alter the physical-mechanical properties of such materials. The same issue was observed when 15% PCM was added to mortar without changing the cement-to-water ratio [5–7]. In addition to the quantity of PCM used, other characteristics must be considered: the chemical nature of the PCM (organic or inorganic) and physical form (such as micro-balls for dispersion, usually incorporated in gypsum [8,9], cementitious mortars, and thin films and plates used for cladding or enveloping surfaces [1,10–13]). Each type and application method may cause different behaviors regarding the internal ambient conservation or release of thermal energy.

Although a few studies on the applications of PCM in mortars and other forms have been reported, research on the in situ behavior of hollow concrete block masonry externally coated with PCM-incorporated mortars is lacking [14–16].

1.2 Infrared thermography (IRT)

Infrared thermography (IRT) is a nondestructive technique used to evaluate existing damage in various components and structures and verify its extension, considering an area or a volume damaged [17–19]. IRT is primarily categorized into two forms: passive thermography (which is conducted under normal operating conditions without thermal or mechanical activation) and active thermography (which involves excitation of the part to be analyzed via heat or mechanical vibration [20–22], potential damage and recovery in facade claddings in historic buildings, or thermal performance in solid brick or rock panels and walls [23–28]). Although thermography has been used to investigate the performance of concrete blocks drilled, the geometry and amount of holes differ considerably worldwide [29], [14].

Furthermore, the behavior of PCM incorporated into the cladding mortar of masonry facades of hollow concrete block walls (HCBWs) has not been investigated. However, studies on the addition of PCM to concrete and its performance, the thermal conductivity of such materials [13,30,31], and cracks on facades investigated via active thermography [24] have been reported.

François et al. [25] reported the use of active thermography in steady-state conditions in an internal room environment [25]. Thermal evaluation of mortar behavior, considering different ratios of constitutive materials, was performed using thermocouples[32]. Gao et al. investigated a few configurations of hollow blocks filled with PCM [33]. Recent studies have demonstrated the effectiveness of IRT in building diagnostics, emphasizing the importance of controlled conditions to minimize the effects of convection and radiation. For example, maintaining a stable environment ensures more accurate thermal measurements by reducing the interference from external factors, such as wind and solar radiation [34].

Additionally, advancements in building diagnostics have highlighted the role of IRT as a noninvasive technology. Tomita and Chew reviewed its applications in detecting delamination and other structural defects and demonstrated its efficacy when measurements were conducted under controlled, stable conditions [35]. Such conditions enhance the ability to accurately visualize and analyze thermal patterns.

In this work, the term cement-lime cladding mortar (CLCM) is used for the facade-cladding mortars, because many formulations for similar purposes exist. The PCM used in the study comprised nano-micro scale balls that were added to the CLCM used experimentally, in two different percentages considering the cement–PCM ratio by mass used to produce the mortar.

2 Materials and methods

To simulate the sun position for the warmest day of 2023 (38.0 °C in September 22rd) over vertical facades at Lat. 21° 00' 17" S and Long. 47° 55' 54" W, a reflector with a pair of 500 W halogen lamps were positioned at an azimuth of 8° of the magnetic North and altitude of 42° from the zenith (or 48° of elevation from the horizon). The normal distance between the center of the HCBW and the projection of the heat source was 217.5 mm.

2.1 Computational approach for predicting thermal behavior over time

Because the evaluation time could be several hours, a software (THERMsyst[®]) for predicting and evaluating the HCBW was developed to investigate the thermal gradient (ΔT) through such walls before the experimental procedure. Thus, to simulate the heat flux through all the HCBW, the 3D model was divided into five plates, where for the plates P1–P5, an initial boundary condition was applied to the white-painted external surface of the CLCM to determine the instantaneous temperature increase at the time when the heat source was released, according to the position described.

All internal faces of P5, the insulated chamber, were protected by a 30-mm-thick ply of expanded polystyrene (EPS).

The theoretical temperature increase was determined using Eq. 1, which was derived from Newton's convective heat transfer [36], Prandtl's convective boundary layer theory [37], Fourier's heat conduction [19], Joule's energy conservation principles [38], and Stefan-Boltzmann radiative heat transfer theories [39] as follows:

$$\Delta T = \frac{\cos(\theta_{azim}) \cdot \cos(\theta_{elev}) \cdot t}{\rho \cdot A \cdot d_{normal} \cdot c} \quad (1)$$

Here, the cosines of β and θ correspond to the elevation and azimuth angle corrections, respectively; t is the duration of heat exposure; ρ is the air density; A is the surface area; d_{normal} is the normal distance from the heat source to the CLCM external face; and c is the specific heat capacity of the air between the heat source and the CLCM. By solving the equation for the initial boundary condition, the software defined the starting temperature acting through the plate P1 of the system, considering that the surface of P1 was coated with white acrylic paint [40].

When the software starts, a window for the input values appears (Fig. 1). When the input is entered and the software is run, it plots the temperature gradient over time.

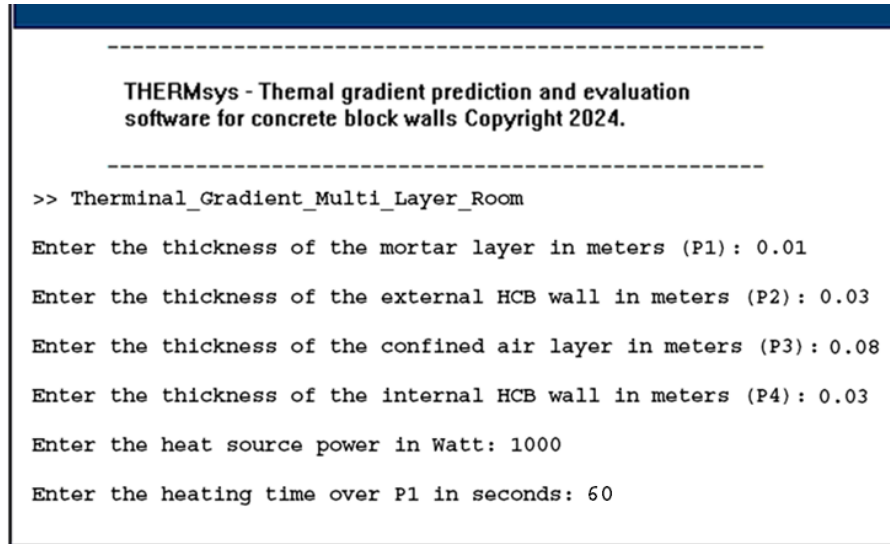


Fig. 1- Software's window to insert input parameters

The algorithm was constructed based on the following assumptions:

- a. All the HCBW materials were perfectly homogeneous and lacked imperfections, voids, or defects;
- b. The thermal flux was transferred equality along the directions 'x,' 'y,' and 'z,' from the Cartesian planes with respect to the local coordinates of the HCBW.
- c. The heat source was constant, and it was distributed over the entire external surface of the HCBW.
- d. The thermal transfer between the insulation box and the exterior was neglected owing to the thermal conductivity of the insulation materials.
- e. It was considered the transient state through all the plates from P1 to P4;
- f. Thirteen distributed points were considered to calculate the average ΔT normal to the plates P1–P5 (as shown in Section 3.3).

Compared to other brands commonly used in previous studies, the brand of PCM used in this work has not been previously used in building applications, such as in mortar mixtures, or in paintings [7]. Thus, the evaluation of thermal properties was based only on the CLCM without the PCM to estimate the time required to increase the internal temperature at the P4 surface.

2.2 Boundary condition for the plate perpendicular to the heat flux

2.2.1 Left boundary (heat source)

The Stefan-Boltzmann law [41] and radiative transfer equations [42] were applied to calculate the loss of

power along the direction of application and the boundary specifications of the material of the heated surface. The field around the heat source and object was insulated (as shown in the infrared experimental procedures), and the left boundary of the first solid plate (P1 described in Fig. 1) was subjected to a radiant heat source. This was modeled using the Neumann boundary condition, which specifies the heat flux at the boundary:

$$-k_{P1} = \frac{\partial T_{P1}}{\partial t} = H(t) \quad (2)$$

Here, $H(t)$ is the time-dependent heat source function (W/m^2), which varies according to the derivative of temperature, while $-k$ is the heat flux normal to the cladding mortar.

2.2.2 Heat conduction in solid plates

Heat conduction through the solid plates (P1, P2, and P4 described in Fig. 1) is governed by the one-dimensional heat equation [7,43]:

$$\rho_{P1,Pn} \cdot c_{P1,Pn} \cdot \frac{\partial T}{\partial t} = \frac{\partial}{\partial x} \left(k_{P1,Pn} \cdot \frac{\partial T}{\partial x} \right) \quad (3)$$

where $\rho_{P1,Pn}$ is the material density of each solid plate P1 up to Pn (kg/m^3); $c_{P1,Pn}$ is the specific heat capacity of the material of each solid plate ($\text{J/kg} \cdot \text{K}$); $k_{P1,Pn}$ is the thermal conductivity of the material of each plate ($\text{W/m} \cdot \text{K}$); $T(x, t)$ is the temperature at position x and time t (s); x is the spatial coordinate along the thickness of the plates (m); and t is the time (s). This equation is derived from the energy balance within an infinitesimal control volume and is a form of Fourier's law of heat conduction, which describes heat flow in response to temperature gradients [1].

2.3 Heat conduction in the air chambers

For each air chamber (P3 described in Fig. 1 and P5 with fixed values in the algorithm), the heat conduction was similarly modeled, but with the properties of air:

$$\rho_{air} \cdot c_{p,air} \cdot \frac{\partial T_{air}}{\partial t} = \frac{\partial}{\partial x} \left(k_{air} \cdot \frac{\partial T_{air}}{\partial x} \right) \quad (4)$$

Here, ρ_{air} , $c_{p,air}$, k_{air} , and $T_{air}(x, t)$ denote the density of the air (kg/m^3), specific heat capacity of air ($\text{J/(kg} \cdot \text{K)}$), thermal conductivity of air ($\text{W/m} \cdot \text{K}$), and temperature of air at position x and time t (s), respectively.

K)), thermal conductivity of air (W/(m-K)), and temperature distribution in the air chamber, respectively. Owing to its lower thermal conductivity, the P3 hollow air chamber acted as an insulating plate, slowing heat transfer between the plates.

2.3.1 Right boundary in P5

The right boundary of the last plate (P5), which was exposed to confined air, was modeled by a Dirichlet boundary condition that sets the temperature at P5, as previously described [43,44], which has a centered opening adjusted for the infrared thermocamera:

$$T_{P4}(D_{4-5}, t) = T_{P5} \quad (5)$$

where D_{4-5} is the distance between the external and internal (EPS) faces of P4 and rear box wall, where the thermocamera is positioned and $T_{Box\ int.}$ is the temperature inside the confined space (K). The algorithm was built following the literature [43–46] and standards related to heat transfer [47,48].

The transient heat conduction problem was solved using the finite difference method by discretizing both space and time. Under these conditions, the temperature was computed for each node created by the software after including input parameters. The software solved the approximate spatial derivatives for heat conduction by central differences using the following equations:

$$\frac{\partial T}{\partial x} \approx \frac{T_{i+1} - T_{i-1}}{2\Delta x} \quad (6)$$

$$\frac{\partial^2 T}{\partial x^2} \approx \frac{T_{i+1} - 2T_i + T_{i-1}}{2\Delta x^2} \quad (7)$$

An explicit forward-time integration method was used to update the temperature of each node over time.

Hence, the time was spatially discretized in steps of Δt as follows:

$$\frac{\partial T}{\partial t} \approx \frac{T_i^{n+1} - T_i^n}{\Delta t} \quad (8)$$

where T_i^n is the temperature at the node i at time step n . Next, the stability of the numerical solution was tested using the Courant-Friedrichs-Lewy method [49], which states that the chosen time step Δt must satisfy the relation:

$$\Delta t \leq \frac{\Delta x^2}{2\alpha} \quad (9)$$

where α is the thermal diffusivity (m^2/s) of the considered material of each plate.

Fig. 2 shows part of the algorithm which includes the material properties; all texts inserted after the “%” sign indicate comments explaining the variables used for the properties of each material.

```
% Material properties for each plate
% (assuming plates are arranged from left to right)
% Plate P1 (Mortar)
k1 = 1.4; % Thermal conductivity in W/(m*K)
rho1 = 1980; % Density in kg/m^3
c1 = 920; % Specific heat capacity in J/(kg*K)

% Plate P2 (Concrete)
k2 = 1.1; % Thermal conductivity in W/(m*K)
rho2 = 2500; % Density in kg/m^3
c2 = 910; % Specific heat capacity in J/(kg*K)

% Plate P3 (Confined air at 300-K - low density)
k3 = 0.026; % Thermal conductivity in W/(m*K)
rho3 = 1.293; % Density in kg/m^3
c3 = 1012; % Specific heat capacity in J/(kg*K)

% Plate P4 (Another type of concrete)
k4 = 1.1; % Thermal conductivity in W/(m*K)
rho4 = 2500; % Density in kg/m^3
c4 = 910; % Specific heat capacity in J/(kg*K)

% Plate P5 (Air at 298-K- representing the interior volume)
k5 = 0.026; % Thermal conductivity in W/(m*K)
rho5 = 1.184; % Density in kg/m^3
c5 = 1006; % Specific heat capacity in J/(kg*K)
```

Fig. 2 – Materials properties used in the algorithm for this research.

The plates P1–P5 in the algorithm refer to the surface positions in the model, as shown in Fig. 3.

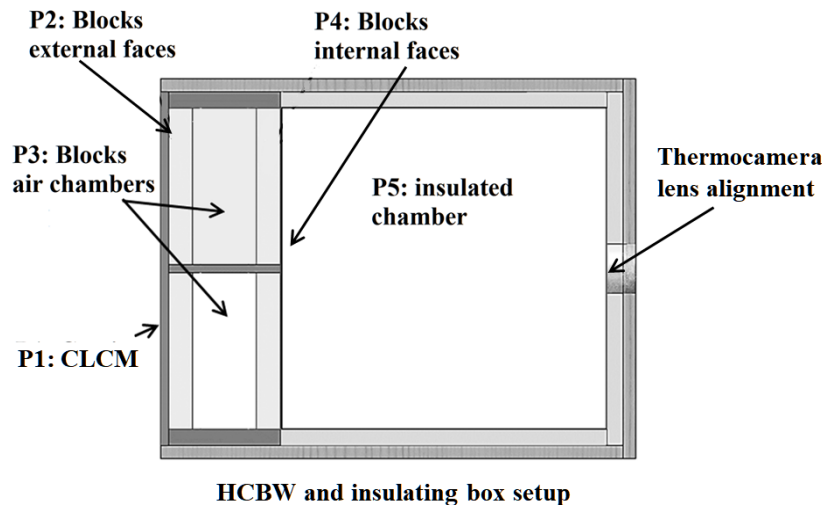


Fig. 3 – HCBW and insulated box assembly model.

- 1 Figure 4 presents the results of the numerical calculations, which show the normal ΔT versus the time
- 2 required to increase the temperature at the face P4 by approximately $1\text{ }^{\circ}\text{C}$ (± 0.5).

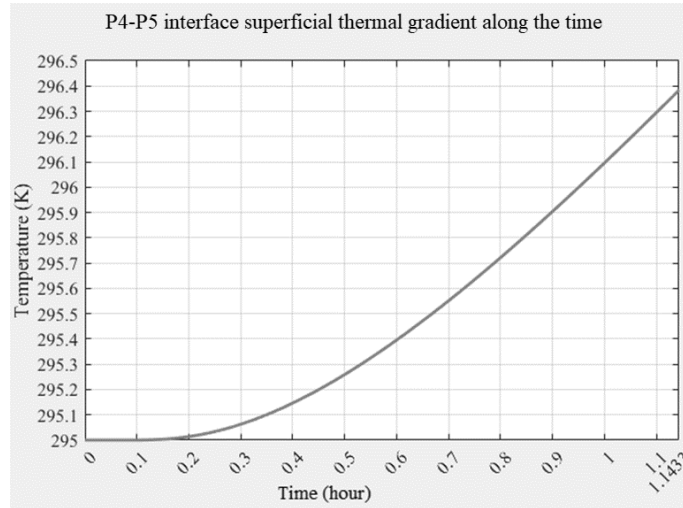


Fig. 4 – Thermal gradient in the normal direction of the HCBW.

- 3 Figure 5 shows ΔT as function of the elapsed time and distance traveled by the heat flux through the plates
- 4 P1 to P4, according to the 13 calculated normal points distributed over the frontal surface.

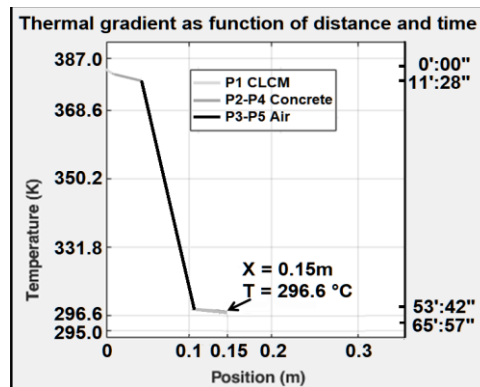


Fig. 5 – Thermal flux in the normal direction of the HCBW.

- 5
- 6 **3 Experimental procedures**
- 7 **3.1 Construction of the HCBW system**
- 8 Three HCBW named SP0, SP4, and SP8 were built. SP0 was the parameter of control, in which PCM was
- 9 not added to the CLCM. In SP4 and SP8, 4% and 8% PCM, respectively, were added to the CLCM, with

respect to the cement mass. The HCBW was built using the blocks shown in Fig. 6, and its geometrical properties are listed in Table 1. The first and second plates comprised one block and two one-half blocks, respectively.

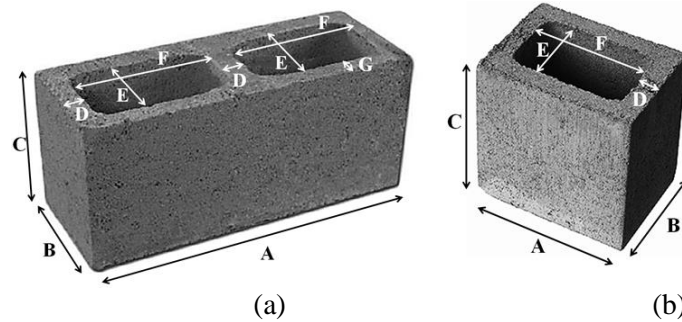


Fig. 6. (a) Block. (b) One-half block.

Table 1. Geometrical properties of hollow concrete blocks used to build the mini-walls.

Type of block	A (mm)	B (mm)	C (mm)	D (mm)	E (mm)	F (mm)	G (mm)
Block	390.2	140.1	190.2	30.1	79.9	2x150.1	29.8
One-half block	190.2	140.3	189.9	30.1	80.1	1x149.8	20.2

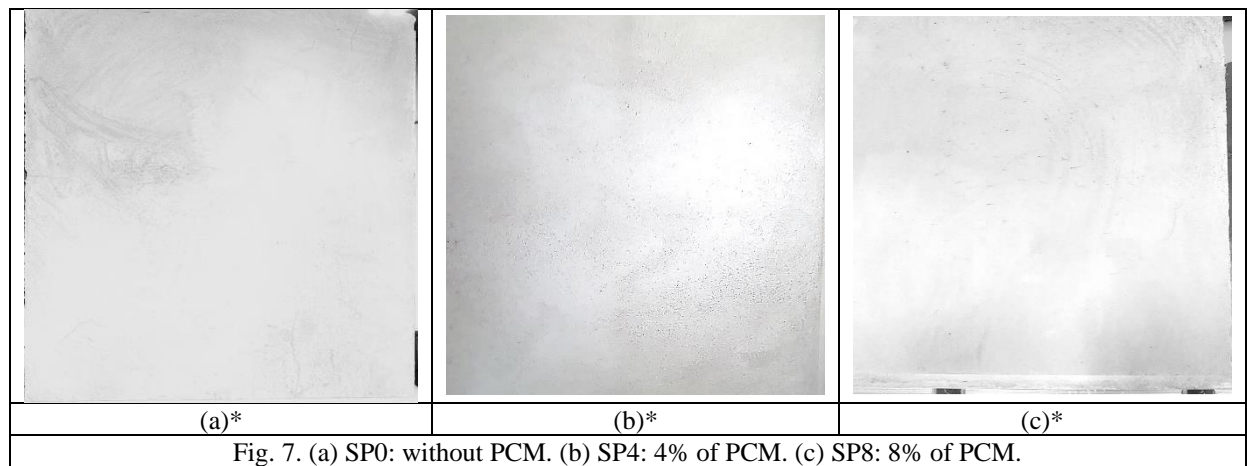
The average density and mass porosity ratio estimated from the total sample of 70 blocks were 2586 kg/m³ and 1.21% respectively. The PCM material used was sold by INSILICO®, Republic of Korea, and its properties are listed in Table 2.

Table 2 – Physical-chemical properties of the PCM

Technical data sheet	
Brand	P-Thermoball 28
Color	white
Average particle diameter	14 – 16 μ m
Heating capacity	170 ~ 175 J/g
Temperature range of phase changing	endothermal range: 26 °C up to 35 °C exothermic range: 26 °C up to 24 °C
Producer	INSILICO® / Rep. of Korea

The CLCM, with a thickness of 11 mm (\pm 1 mm), was applied 24 hours after building the HCBW, and the

specimens were rested for 48 h in the laboratory at a temperature of 22 °C and relative humidity (RH) of 45% . Figures 7 (a)–(c) show SP0, SP4, and SP8, respectively.



*The difference of the gray tonality is because of the camera position regarding the ambient light.

The analysis began at 17:00:00 and each specimen was analyzed on consecutive days. This approach ensured stable humidity during analysis in summer, because of the thermal amplitude owing to summer tempests between 10:00h and 15:00h, which causes the average temperature of 39 °C to decrease to 14 °C in a few minutes.

3.2 Experimental procedures

Before acquiring thermal images, the temperature and RH were measured using a KASVI thermo-hygrometer (model K29-5070H) positioned at the center of the HCBW. This was to ensure that a temperature of 22 °C (± 0.5 °C) and RH of 45% ($\pm 0.5\%$) were attained by the air conditioning system. A thermocamera (FLIR, model Vision A320) was used for the analysis, and it was positioned at the center of the rear face of the insulating box (Fig. 8), which covered all the specimen walls, except where the CLCM was cladded. For each HCBW, one box was built, and the HCBW were enveloped by them, except on the external face. The heat source was positioned exactly as calculated using Eq. (1) and sealed with silicone rubber at all the contact faces, except for the insulating box of the reflector.

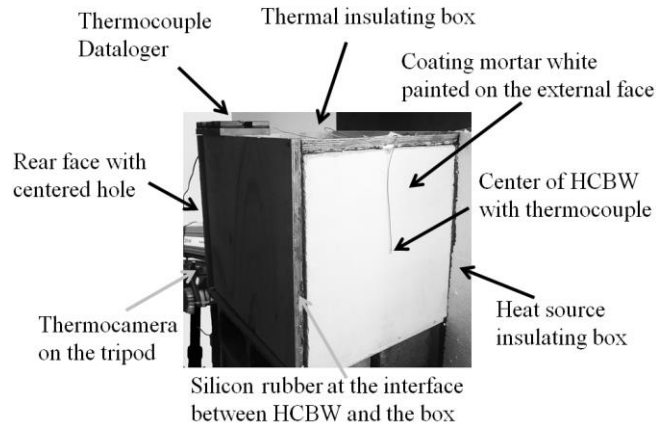


Fig. 8 Setup (SP0) to conduct the analysis

3.3 Infrared thermocamera analysis

Upon rectifying the heat source, as previously indicated, a protective casing was placed around the sides, top, and bottom of the heating surface to prevent external disturbances. Fig. 9 depicts the 3D model, showing the heat source's position in relation to the elevation and azimuth angles used in the experiments, and featuring a protective box designed to prevent airflow disturbances.

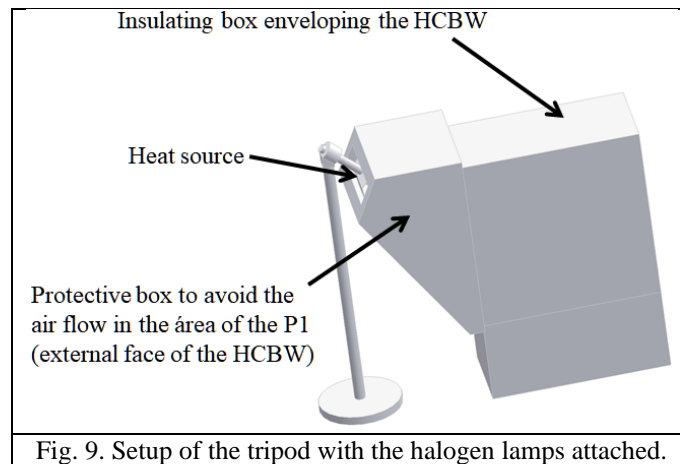


Fig. 9. Setup of the tripod with the halogen lamps attached.

The heat source (1000 W) was turned on for 6 s, covering the entire external face of the CLCM, and then turned off; simultaneously, the thermocamera acquired thermograms at a frequency of 4 Hz. Nine thermal images (Ti1 to Ti9) were acquired along the time up to increase the temperature by 1.5 °C (± 0.2 °C). Fig. 10 shows the quoted marks over the HCBW at the surface of P4. The thermocamera's software was able to record the temperature for the total area focused, considering the image's pixel resolution of 640 x 480.

1 Thus, the 13 Spot-points (Sp1 to Sp13) were measured for each specimen.

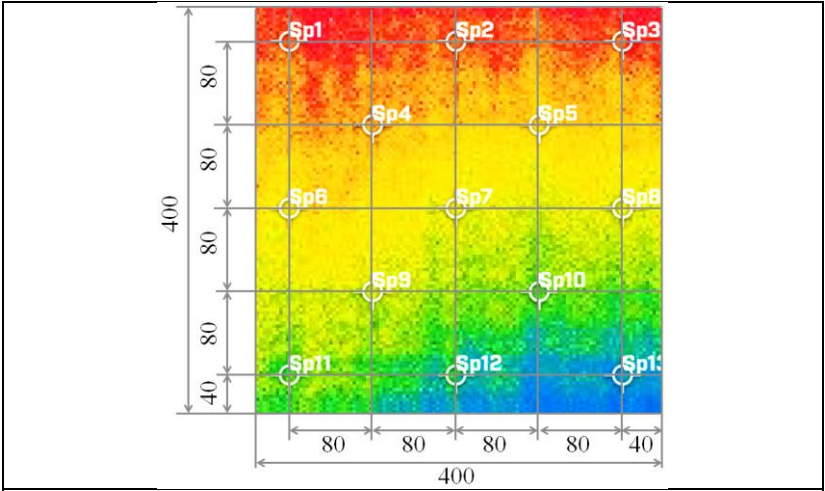


Fig. 10. Measuring thermal points over the thermograms of all specimens.

2
3 Each image was taken at the time when a significant temperature gradient was observed by the
4 thermocamera during the acquisition time. Fig. 11 shows the plotted temperatures for the 13 Sp for the
5 nine images taken of SP0.

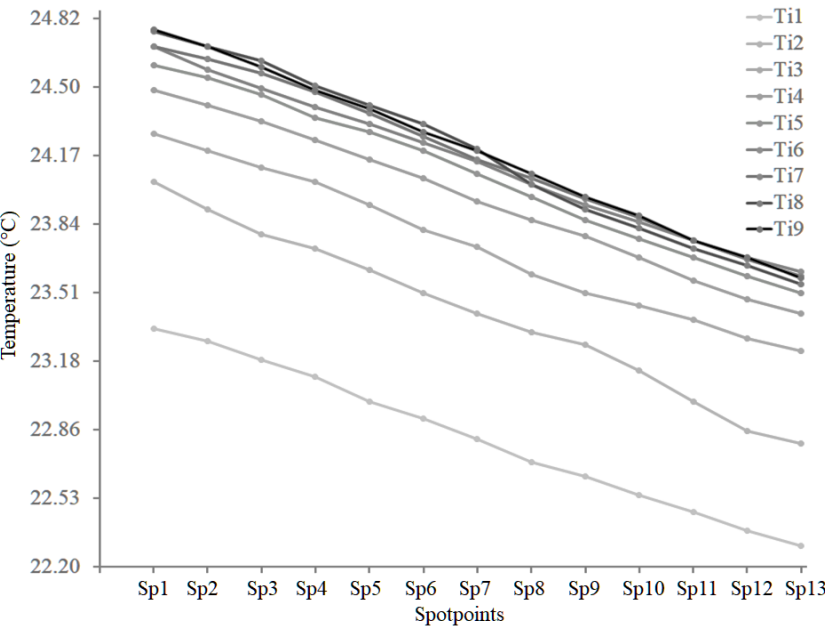


Fig. 11. One of thermogram map taken during the experiment for the three specimens.

6 Tables 3, 4, and 5 present the total instantaneous temperature at each Sp with respect to the time when the
7 thermocamera acquired the fixed Ti. The first and second times were almost identical for all the specimens

and corresponded to 1800 and 2500 s, respectively. Subsequently, according to the temperature elevation, each image was captured at a different time for each specimen.

Table 3. Thermal variation along the time and thermal points positions for the SP0.

Point	t_0	t_1800	t_2700	t_3300	t_3600	t_3793	t_3927	t_4004	t_4059
Sp1	23.34	24.04	24.27	24.48	24.60	24.69	24.69	24.76	24.77
Sp2	23.28	23.91	24.19	24.41	24.54	24.58	24.63	24.69	24.69
Sp3	23.19	23.79	24.11	24.33	24.46	24.49	24.56	24.62	24.59
Sp4	23.11	23.72	24.04	24.24	24.35	24.40	24.47	24.50	24.48
Sp5	22.99	23.62	23.93	24.15	24.28	24.32	24.37	24.41	24.39
Sp6	22.91	23.51	23.81	24.06	24.19	24.23	24.26	24.32	24.28
Sp7	22.81	23.41	23.73	23.95	24.08	24.14	24.15	24.20	24.19
Sp8	22.70	23.32	23.60	23.86	23.97	24.03	24.06	24.03	24.08
Sp9	22.63	23.26	23.51	23.78	23.86	23.93	23.96	23.91	23.97
Sp10	22.54	23.14	23.45	23.68	23.77	23.85	23.87	23.82	23.88
Sp11	22.46	22.99	23.38	23.57	23.68	23.76	23.76	23.72	23.76
Sp12	22.37	22.85	23.29	23.48	23.59	23.68	23.67	23.64	23.68
Sp13	22.30	22.79	23.23	23.41	23.51	23.61	23.59	23.55	23.58
Average	22.82	23.41	23.73	23.95	24.07	24.13	24.16	24.17	24.18
SD	0.29	0.33	0.30	0.30	0.31	0.30	0.31	0.36	0.33

Table 4. Thermal variation along the time and thermal points positions for the SP4.

Point	t_0	t_1800	t_2700	t_3600	t_4226	t_4411	t_4532	t_4627	t_4701
Sp1	23.32	23.91	24.21	24.46	24.64	24.64	24.69	24.69	24.71
Sp2	23.24	23.86	24.16	24.41	24.57	24.61	24.60	24.64	24.62
Sp3	23.15	23.77	24.09	24.34	24.48	24.52	24.51	24.57	24.52
Sp4	23.07	23.64	23.97	24.28	24.39	24.41	24.42	24.48	24.44
Sp5	23.02	23.59	23.85	24.21	24.30	24.32	24.31	24.39	24.35
Sp6	22.96	23.50	23.73	24.10	24.21	24.24	24.22	24.27	24.26
Sp7	22.85	23.39	23.64	23.96	24.11	24.15	24.16	24.17	24.16
Sp8	22.78	23.31	23.56	23.86	23.99	24.07	24.06	24.08	24.09
Sp9	22.67	23.19	23.47	23.79	23.90	23.96	23.96	23.91	23.97

Sp10	22.59	23.09	23.41	23.70	23.82	23.84	23.87	23.85	23.88
Sp11	22.48	22.98	23.32	23.59	23.74	23.75	23.79	23.76	23.81
Sp12	22.39	22.89	23.21	23.48	23.66	23.67	23.73	23.70	23.73
Sp13	22.31	22.76	23.16	23.41	23.59	23.63	23.64	23.64	23.64
Average	22.83	23.38	23.68	23.97	24.11	24.14	24.15	24.17	24.17
SD	0.27	0.31	0.30	0.31	0.30	0.29	0.29	0.32	0.29

Table 5. Thermal variation along the time and thermal points positions for the SP8.

Point	t_0	t_1800	t_2400	t_3600	t_4200	t_4800	t_5672	t_5767	t_5841
Sp1	23.34	23.75	24.23	24.35	24.62	24.62	24.64	24.67	24.68
Sp2	23.22	23.73	24.13	24.32	24.55	24.57	24.57	24.60	24.58
Sp3	23.13	23.64	24.04	24.27	24.41	24.50	24.49	24.52	24.49
Sp4	23.05	23.59	23.92	24.23	24.37	24.41	24.40	24.43	24.38
Sp5	22.96	23.49	23.79	24.14	24.23	24.32	24.26	24.33	24.29
Sp6	22.88	23.46	23.69	24.02	24.12	24.21	24.17	24.22	24.21
Sp7	22.80	23.38	23.57	23.89	24.01	24.13	24.11	24.13	24.12
Sp8	22.72	23.27	23.53	23.81	23.93	24.02	24.02	24.01	24.05
Sp9	22.64	23.21	23.42	23.75	23.87	23.91	23.95	23.91	23.94
Sp10	22.57	23.12	23.34	23.69	23.77	23.79	23.86	23.83	23.83
Sp11	22.49	22.99	23.30	23.53	23.66	23.71	23.77	23.75	23.76
Sp12	22.41	22.90	23.21	23.45	23.60	23.65	23.69	23.66	23.71
Sp13	22.36	22.78	23.11	23.34	23.57	23.57	23.60	23.57	23.65
Average	22.81	23.33	23.64	23.91	24.05	24.11	24.12	24.12	24.13
SD	0.26	0.26	0.30	0.29	0.30	0.31	0.28	0.31	0.28

When the ΔT of the analyzed specimens reached the predetermined limiting value, the data were computed and grouped according to the specimen considered. Next, the average ΔT for the specimen was determined for each thermogram considered. Table 6 summarizes the results for each specimen converted to minutes and seconds format (mm:ss).

Table 6. Average ΔT by percentage of PCM mixed in each specimen CLCM.

SP0		SP4		SP8	
Time (mm:ss)	Temp. ($^{\circ}\text{C}$)	Time (mm:ss)	Temp. ($^{\circ}\text{C}$)	Time (mm:ss)	Temp. ($^{\circ}\text{C}$)
0:00	22.82	0:00	22.83	0:00	22.81
30:00	23.41	30:00	23.38	30:00	23.33
45:00	23.73	45:00	23.68	45:00	23.64
55:00	23.95	60:00	23.97	60:00	23.91
60:00	24.07	70:16	24.11	75:00	24.05
63:08	24.13	73:19	24.14	90:00	24.11
65:16	24.16	75:19	24.15	94:19	24.12
66:26	24.17	77:04	24.17	96:04	24.13
67:23	24.18	78:13	24.17	97:13	24.13
Total time	ΔT	Total time	ΔT	Total time	ΔT
67:23	1.36	78:13	1.33	97:13	1.32

4 Results and discussion

4.1 Software simulation

After the experiments, the software was run again; however, the maximum time was identical to the experimental duration for SP0. Both gradients were compared to determine if the prediction software could be used together with the IRT in future experiments to predict the amount of PCM added to CLCMs.

The simulated and experimental ΔT for SP0 were 1.34 $^{\circ}\text{C}$ and 1.36 $^{\circ}\text{C}$, respectively, which indicated that the experimental ΔT 1.5% higher than the simulated result. Similarly, for the SP4 the ΔT was 1.30 $^{\circ}\text{C}$ from the software against 1.34 $^{\circ}\text{C}$ from the experiment, which was 3% higher than the simulated result.

Finally, for the SP8, the ΔT (1.32 $^{\circ}\text{C}$) was 2.3% greater than the software result (1.29 $^{\circ}\text{C}$). Such a difference is negligible and may be attributed to the differences between the real specimens (which contain intrinsic invisible defects and voids) and the model (which considered all the materials as perfectly homogeneous, without voids, dislocations, or concentrations of sand, lime, or cement, as may occur in real CLCMs).

4.2 Experimental analysis

The comparative results of the experiments (tables 3, 4, and 5) showed all Sp over the surface of P4, for the three specimens, which were measured by the IRT by the nine images acquired during analysis, from which the average results were plotted by each specimen (Fig. 12). Therefore, the results showed the Sp average temperatures increasing during the nine Ti acquired. Thus, the ΔT of each specimen corresponds to such temperature.

To evaluate the convergence of the results achieved by each Ti showed in Tables 3 to 5, was applied the Chauvenet criterion, which is used statistical method for outlier detection in scientific and engineering contexts, where data precision is paramount. Its reliance on probabilistic thresholds ensures consistency, while recent advancements have enhanced its robustness for use in datasets with high levels of contamination [50]. The applied criterion [51] is satisfied by each specimen's spot-point temperatures (Tables 3, 4, and 5), as shown in supplementary materials.

The ΔT increasing along the experiments are presented in Fig. 12, where the plotted curves versus time to increase the temperature at the surface of P4 followed a quasi-linear parallel pattern up to 35 min.

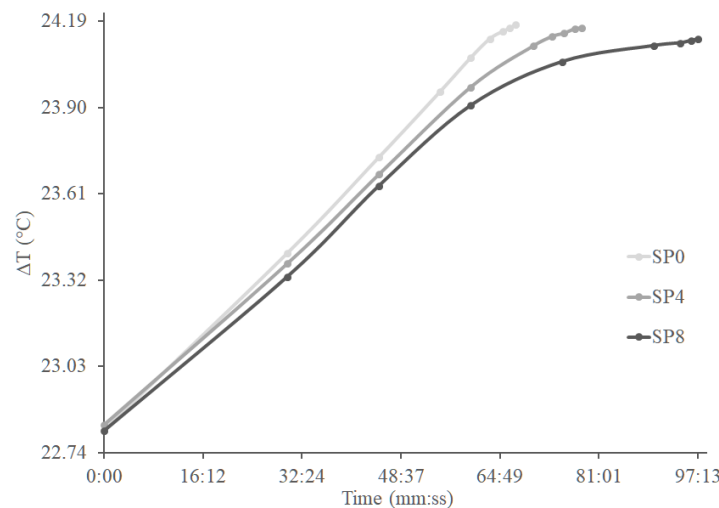


Fig. 12. Average ΔT versus time by specimen.

Next, SP0, without PCM added to the CLCM, increased at a higher rate than SP4 and SP8, which continued almost parallel for 50 minutes. In contrast, the ΔT of SP8 diminished at an increasing rate, indicating that the decelerating rate of the heat flux through the HCBW was higher than that for SP4.

Hence, although the limit of ΔT was determined for all the experiments, the incorporation of PCM into the CLCM mixture increased the time required to increase the same thermal gradient in the three specimens. Since the three ΔT values were not identical among the specimens, to determine the actual variation that occurred, ΔT was normalized (ΔT_{NORM}) by the specimen with the greater variation: 1.36 °C (SP0). In this way, the time required for it to increase by 1 unity for SP4 with respect to SP0 was over 10%. Similarly, for SP8 with respect to SP0, the time required to reach 1 unity was more than 33% compared to the specimen without PCM, as shown in Table 7. Therefore, SP4 should take approximately 2 minutes less for an increase of 1 degree, while SP8 should take approximately 1.5 minute more than the experimental time.

Table 7. Normalized thermal gradient as a function of time.

Temperature (°C)	Time (mm:ss)	%
1.00	67:00	-
1.02	76:17	10.2
0.97	98:51	33.5

Because the time of exposure proposed was equivalent to 15:00 h in the middle of spring, the temperature of SP8 increased by 1.32 °C after 97 min. However, a few factors must be considered.

- a. Solar azimuth and elevation angles exhibit diurnal variation, resulting in a reduction of solar heating capacity between 15:00 h and sunset (18:05 h, at the specified date, latitude, and longitude).
- b. The shadows of other buildings over the facades, which must be considered in urban centers, were neglected in the present study.

Because all the three experimental curves exhibited a decelerating trend in ΔT , it could be inferred that as the day advanced, the curves would present the inversion of the concavity, indicating decreasing temperatures, according to the time mentioned for the heat source position in terms of azimuth and elevation with respect to the HCBW. Confirming the previous work [7], the temperature could be stabilized by reducing the power source during the day, owing to the tendency of the PCM to retain the energy for a few hours before releasing it into the cooler environment (internal or external).

5 Conclusions

This study theoretically and experimentally evaluated the ability of the IRT to evaluate the behavior of PCM mixed in CLCMs to reduce the thermal gradient incident on HCBW facades, on the hottest day of the year, at a typical latitude in the tropical zone. The procedure adopted for acquiring ΔT via IRT was effective and proved that the proposed method was suitable for evaluating the behavior of PCM.

Nevertheless, the CLCM containing PCM should be evaluated regarding the loss of adhesion and the occurrence of cracks caused by excessive shrinkage during the curing process, in real conditions of application on facades. PCM present a practical approach for reducing the thermal gradient in real conditions, particularly for reducing the energy spent for artificial internal cooling systems in multistory commercial buildings or in homes in tropical regions (Fig. 13), where the income of almost 60% of the population is as low as US\$220.0/month [52].

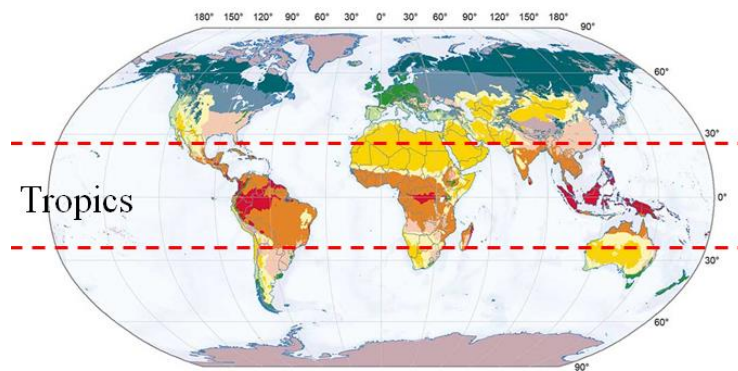


Fig. 13. Countries in the tropical region on the earth.

This study's proposed IRT technique is well-suited for investigating novel functional building materials aimed at mitigating building energy costs. These materials include, but are not limited to, external CLCMs (in areas with spring temperatures exceeding 35°C at 15:00 h), paints containing the researched PCM, and polymeric facade cladding incorporating the studied PCM.

Glossary

c	specific heat capacity
CLCM(s)	cement-lime cladding mortar(s)

EPS	expanded polystyrene
HCBW(s)	hollow concrete block wall(s)
$H(t)$	heat flux as a function of time
K	Kelvin
k	heat flux through a specific direction
IRT	infrared thermography
P1 to P5	thermal plates formed by the mortar, external block wall, confined air, second block wall, and insulating box confined air, respectively
PCM	phase change material
SP0	specimen in which the cladding mortar has no PCM mixed in
SP4	specimen in which there is 4% by mass of PCM mixed in the mortar
SP8	specimen in which there is 8% by mass of PCM mixed in the mortar
Sp ₁ to Sp ₁₃	Spot-points marked by the IRT software to take the instantaneous temperature
t	time
T	temperature
Ti1 to Ti9	Thermal images taken from the continuous acquisition of IRT system
T_i^n	temperature considered in a specific node of the algorithm
ΔT	thermal gradient from room temperature up to reach 1.5 °C (± 0.2 °C)
ΔT_{NORM}	normalized thermal gradient by SP0
α	thermal diffusivity
β	azimuth angle
θ	elevation angle
ρ	specific mass of the considered material

1

2 **Author contributions: CRediT**

3 Both authors contributed equally to this work.

4 **Funding:** This research did not receive any specific grant from funding agencies in the public,

5 commercial, or not-for-profit sectors.

Acknowledgments

The authors thank the LISTLAB laboratory and the Civil Engineering students from the State University of Londrina for assisting with the IRT and for preparing the raw materials of the specimens.

The authors thank Editage for English language editing.

REFERENCES

- [1] Cabeza LF, Ürge-Vorsatz D. The role of buildings in the energy transition in the context of the climate change challenge. *Glob Transitions* 2020;2:257–60.
<https://doi.org/10.1016/j.glt.2020.11.004>.
- [2] Al-Yasiri Q, Szabó M. Incorporation of phase change materials into building envelope for thermal comfort and energy saving: A comprehensive analysis. *J Build Eng* 2021;36.
<https://doi.org/10.1016/j.jobbe.2020.102122>.
- [3] Ürge-Vorsatz D, Cabeza LF, Serrano S, Barreneche C, Petrichenko K. Heating and cooling energy trends and drivers in buildings. *Renew Sustain Energy Rev* 2015;41:85–98.
<https://doi.org/10.1016/j.rser.2014.08.039>.
- [4] Zhan H, Mahyuddin N, Sulaiman R, Khayatian F. Phase change material (PCM) integrations into buildings in hot climates with simulation access for energy performance and thermal comfort: A review. *Constr Build Mater* 2023;397:132312. <https://doi.org/10.1016/j.conbuildmat.2023.132312>.
- [5] Cunha S, Aguiar J, Pacheco-Torgal F. Effect of temperature on mortars with incorporation of phase change materials. *Constr Build Mater* 2015;98:89–101.
<https://doi.org/10.1016/j.conbuildmat.2015.08.077>.
- [6] Cunha S, Lima M, Aguiar JB. Influence of adding phase change materials on the physical and mechanical properties of cement mortars. *Constr Build Mater* 2016;127:1–10.
<https://doi.org/10.1016/j.conbuildmat.2016.09.119>.
- [7] Fabiche MNF, Virga A, Ortenzi A. Thermal Performance Investigation of Phase Change Materials in Concrete Blocks Masonry. *Mater Res* 2023;26:1–7. <https://doi.org/10.1590/1980-5373-MR-2023-0068>.

- [8] Lai CM, Chen RH, Lin CY. Heat transfer and thermal storage behaviour of gypsum boards incorporating micro-encapsulated PCM. *Energy Build* 2010;42:1259–66.
<https://doi.org/10.1016/j.enbuild.2010.02.018>.
- [9] El-Bichri FZ, Sobhy I, Bouchefra I, Benhamou B, Chehouani H, Mghazli MO. Assessment of the impact of construction materials on the building's thermal behaviour and indoor thermal comfort in a hot and semi-arid climate. *Adv Build Energy Res* 2022;16:711–35.
<https://doi.org/10.1080/17512549.2022.2096692>.
- [10] Baert G, Hoste S, De Schutter G, De Belie N. Reactivity of fly ash in cement paste studied by means of thermogravimetry and isothermal calorimetry. *J Therm Anal Calorim* 2008;94:485–92.
<https://doi.org/10.1007/s10973-007-8787-z>.
- [11] Cunha S, Aguiar JB, Ferreira VM, Tadeu A. Influence of the type of phase change materials microcapsules on the properties of lime-gypsum thermal mortars. *Adv Eng Mater* 2014;16:433–41.
<https://doi.org/10.1002/adem.201300278>.
- [12] Cunha S, Silva M, Aguiar J. Behavior of cementitious mortars with direct incorporation of non-encapsulated phase change material after severe temperature exposure. *Constr Build Mater* 2020;230:117011. <https://doi.org/10.1016/j.conbuildmat.2019.117011>.
- [13] Dehmous M, Franquet E, Lamrous N. Mechanical and thermal characterizations of various thermal energy storage concretes including low-cost bio-sourced PCM. *Energy Build* 2021;241:110878.
<https://doi.org/10.1016/j.enbuild.2021.110878>.
- [14] Caruana C, Yousif C, Bacher P, Buhagiar S, Grima C. Determination of thermal characteristics of standard and improved hollow concrete blocks using different measurement techniques. *J Build Eng* 2017;13:336–46. <https://doi.org/10.1016/j.job.2017.09.005>.
- [15] Sassine E, Cherif Y, Dgheim J, Antczak E. Investigation of the mechanical and thermal performances of concrete hollow blocks. *SN Appl Sci* 2020;2:1–17.
<https://doi.org/10.1007/s42452-020-03881-x>.
- [16] Hamidi Y, Aketouane Z, Malha M, Bruneau D, Bah A, Goiffon R. Integrating PCM into hollow

- brick walls: Toward energy conservation in Mediterranean regions. *Energy Build* 2021;248:111214. <https://doi.org/10.1016/j.enbuild.2021.111214>.
- [17] Georges MP. Speckle interferometry in the long-wave infrared for combining holography and thermography in a single sensor: applications to nondestructive testing: The FANTOM Project. *Opt Meas Syst Ind Insp IX* 2015;9525:95251L. <https://doi.org/10.1117/12.2191133>.
- [18] Georges M, Sraibr C, Menner P, Koch J, Dillenz A. Thermography and Shearography Inspection of Composite Hybrid Sandwich Structure Made of CFRP and GFRP Core and Titanium Skins 2018;484. <https://doi.org/10.3390/icem18-05384>.
- [19] Guo T, Sang G, Zhang Y, Cui X, Zhang L. Study on the dynamic thermal response of phase change material integrated wall under indoor-outdoor dual thermal disturbances. *J Energy Storage* 2024;85:111059. <https://doi.org/10.1016/j.est.2024.111059>.
- [20] Maldague XP V. Nondestructive evaluation of materials by infrared thermography. 1st ed. Québec: Springer-Verlag; 1993. <https://doi.org/10.1007/978-1-4471-1995-1>.
- [21] Netzelmann U, Walle G, Lugin S, Ehlen A, Bessert S, Valeske B. Induction thermography: principle, applications and first steps towards standardisation. *Quant Infrared Thermogr J* 2016;13:170–81. <https://doi.org/10.1080/17686733.2016.1145842>.
- [22] Budzier H, Gerlach G. Active Thermography. In: Ida N, Meyendorf N, editors. *Handb. Adv. Nondestruct. Eval.*, Springer; 2019, p. 1–23. https://doi.org/https://doi.org/10.1007/978-3-319-26553-7_13.
- [23] Barreira E, de Freitas VP. Evaluation of building materials using infrared thermography. *Constr Build Mater* 2007;21:218–24. <https://doi.org/10.1016/j.conbuildmat.2005.06.049>.
- [24] Bauer E, Pavón E, Oliveira E, Pereira CHF. Facades inspection with infrared thermography: cracks evaluation. *J Build Pathol Rehabil* 2016;1. <https://doi.org/10.1007/s41024-016-0002-9>.
- [25] François A, Ibos L, Feuillet V, Meulemans J. In situ measurement method for the quantification of the thermal transmittance of a non-homogeneous wall or a thermal bridge using an inverse technique and active infrared thermography. *Energy Build* 2021;233.

1 <https://doi.org/10.1016/j.enbuild.2020.110633>.

- 2 [26] Paoletti D, Ambrosini D, Sfarra S, Bisegna F. Preventive thermographic diagnosis of historical
3 buildings for consolidation. *J Cult Herit* 2013;14:116–21.

4 <https://doi.org/10.1016/j.culher.2012.05.005>.

- 5 [27] Resende MM, Gambare EB, Silva LA, Cordeiro Y de S, Almeida E, Salvador RP. Infrared thermal
6 imaging to inspect pathologies on façades of historical buildings: A case study on the Municipal
7 Market of São Paulo, Brazil. *Case Stud Constr Mater* 2022;16:e01122.

8 <https://doi.org/10.1016/j.cscm.2022.e01122>.

- 9 [28] Tardy F. A review of the use of infrared thermography in building envelope thermal property
10 characterization studies. *J Build Eng* 2023;75:106918. <https://doi.org/10.1016/j.jobe.2023.106918>.

- 11 [29] Babaharra O, Choukairy K, Faraji H, Khallaki K, Hamdaoui S, Bahammou Y. Thermal
12 performance analysis of hollow bricks integrated phase change materials for various climate zones.
13 *Heat Transf* 2024;53:2148–72. <https://doi.org/10.1002/htj.23031>.

- 14 [30] Berardi U, Gallardo AA. Properties of concretes enhanced with phase change materials for
15 building applications. *Energy Build* 2019;199:402–14.

16 <https://doi.org/10.1016/j.enbuild.2019.07.014>.

- 17 [31] Fenollera M, Míguez JL, Goicoechea I, Lorenzo J. Experimental study on thermal conductivity of
18 self-compacting concrete with recycled aggregate. *Materials (Basel)* 2015;8:4457–78.

19 <https://doi.org/10.3390/ma8074457>.

- 20 [32] Cunha S, Aguiar J, Ferreira V, Tadeu A. Mortars based in different binders with incorporation of
21 phase-change materials: Physical and mechanical properties. *Eur J Environ Civ Eng*
22 2015;19:1216–33. <https://doi.org/10.1080/19648189.2015.1008651>.

- 23 [33] Gao Y, He F, Meng X, Wang Z, Zhang M, Yu H, et al. Thermal behavior analysis of hollow bricks
24 filled with phase-change material (PCM). *J Build Eng* 2020;31:101447.

25 <https://doi.org/10.1016/j.jobe.2020.101447>.

- 26 [34] Kim H, Lamichhane N, Kim C, Shrestha R. Innovations in Building Diagnostics and Condition

- Monitoring: A Comprehensive Review of Infrared Thermography Applications. *Build* 2023, Vol 13, Page 2829 2023;13:2829. <https://doi.org/10.3390/BUILDINGS13112829>.
- [35] Chew M; YLA, Qiu L, Liang Y, Khodaei ZS, Tomita K, Yit M, et al. A Review of Infrared Thermography for Delamination Detection on Infrastructures and Buildings. *Sensors* 2022, Vol 22, Page 423 2022;22:423. <https://doi.org/10.3390/S22020423>.
- [36] Zhao B. Integrity of Newton's cooling law based on thermal convection theory of heat transfer and entropy transfer. *Sci Reports* 2022 121 2022;12:1–16. <https://doi.org/10.1038/s41598-022-18961-8>.
- [37] Amran MF, Sultan SM, Tso CP. A Comprehensive Review of Mixed Convective Heat Transfer in Tubes and Ducts: Effects of Prandtl Number, Geometry, and Orientation. *Process* 2024, Vol 12, Page 2749 2024;12:2749. <https://doi.org/10.3390/PR12122749>.
- [38] Young J. Heat, work and subtle fluids: a commentary on Joule (1850) 'On the mechanical equivalent of heat.' *Philos Trans R Soc A Math Phys Eng Sci* 2015;373. <https://doi.org/10.1098/RSTA.2014.0348>.
- [39] Lévesque L, Guan K, Jiang Y, Sun C, Yu H, Torres JH, et al. Law of cooling, heat conduction and Stefan-Boltzmann radiation laws fitted to experimental data for bones irradiated by CO2 laser. *Biomed Opt Express* 2014;5:701. <https://doi.org/10.1364/BOE.5.000701>.
- [40] Simpson A, Fitton R, Rattigan IG, Marshall A, Parr G, Swan W. Thermal performance of thermal paint and surface coatings in buildings in heating dominated climates. *Energy Build* 2019;197:196–213. <https://doi.org/10.1016/J.ENBUILD.2019.04.027>.
- [41] Hristov J. Explicit Analytical Solutions by Improved Integral-Balance Method 2018;22:777–88.
- [42] Amamou H, Bois A, Ferhat B. Procedure to Solve the One-Dimensional Radiative Transfer Equation (1D-RTE) of an Ionized Medium Using Spatial Discretization and an Iterative Process. *Appl Spectrosc Pract* 2024;2:1–8. <https://doi.org/10.1177/27551857241228616>.
- [43] Hsu HP, Chang JR, Weng CY, Huang CJ. An Analytic Solution for 2D Heat Conduction Problems with Space–Time-Dependent Dirichlet Boundary Conditions and Heat Sources. *Axioms* 2023;12.

1 <https://doi.org/10.3390/axioms12070708>.

- 2 [44] Käufer T, Vieweg PP, Schumacher J, Cierpka C. Thermal boundary condition studies in large
3 aspect ratio Rayleigh–Bénard convection. *Eur J Mech B/Fluids* 2023;101:283–93.

4 <https://doi.org/10.1016/j.euromechflu.2023.06.003>.

- 5 [45] Bergman TL, Lavine AS. Fundamentals of heat and mass transfer. 8th ed. Hoboken: Wiley; 2019.

- 6 [46] Ozel M. Effect of insulation location on dynamic heat-transfer characteristics of building external
7 walls and optimization of insulation thickness. *Energy Build* 2014;72:288–95.

8 <https://doi.org/10.1016/J.ENBUILD.2013.11.015>.

- 9 [47] ASHRAE. ASHRAE Handbook 2021 Fundamentals. 2021st ed. Atlanta: 2021.

- 10 [48] International Standard Organisation. ISO 6946 - Building components and building elements -
11 Thermal resistance and thermal transmittance - Calculation methods 2017:15.

- 12 [49] Raeth M, Hallatschek K. Surprisingly tight Courant-Friedrichs-Lewy condition in explicit high-
13 order Arakawa schemes. *Phys Fluids* 2024;36:105167. <https://doi.org/10.1063/5.0223009/3317206>.

- 14 [50] Maples MP, Reichart DE, Konz NC, Berger TA, Trotter AS, Martin JR, et al. Robust Chauvenet
15 Outlier Rejection. *Astrophys J Suppl Ser* 2018;238:2. <https://doi.org/10.3847/1538-4365/AAD23D>.

- 16 [51] Ortenzi A, Chinelatto M. Chauvenet criterion applied to thermal data acquired. 2025.

17 <https://doi.org/https://doi.org/10.17605/OSF.IO/9R7T5>.

- 18 [52] IBGE - Instituto Brasileiro de Geografia e Estatística. Per capita income in Brazil - 2023 (in
19 Portuguese). Brasilia: 2024.